Evolution of microstructure and mechanical properties as a consequence of tensile creep strain of NNS-HIPped nickel-based superalloy

Journal of Materials Research and Technology 42 (2026) 2826–2837

Contents lists available at ScienceDirect

Journal of Materials Research and Technology

journal homepage: www.elsevier.com/locate/jmrt

Evolution of microstructure and mechanical properties as a consequence of tensile creep strain of NNS-HIPped nickel-based superalloy

Jehanzaib Anwar *, Emilio Bassini, Giulio Marchese, Sara Biamino, Daniele Ugues

Department of Applied Science and Technology (DISAT), Politecnico di Torino, Corso Duca degli Abruzzi 24, 10129, Torino, Italy

ARTICLE INFO

Keywords:
Hot isostatic pressing
Near net shape
Tensile creep strain
Nickel super alloy
Astroloy
Powder metallurgy

ABSTRACT

Nickel superalloys are being widely used in high-temperature applications such as aerospace and power generation due to their excellent mechanical properties. However, long-term exposure to high temperatures under continuous stress leads to microstructural and mechanical degradation, making it unfit for service. Therefore, this study analyzes the creep behavior of astroloy fabricated via near-net shape hot isostatic pressing (NNS–HIP). NNS-HIP is a powder metallurgy technique enabling precise component fabrication that is difficult to manufacture through conventional methods by densifying loosened powders in a pre-designed capsule under high temperature and isostatic pressure with the help of compressed inert gas. Creep tests were conducted at different temperatures (650, 760 & 820 °C) and stress conditions. Optical and scanning electron microscopy (SEM) analysis revealed that increasing temperature influences the transition of grain boundary precipitates from discontinuous to interconnected morphologies, facilitating intergranular crack initiation and propagation. Additionally, hardness testing demonstrated a direct correlation between excessive precipitate coarsening and reduced mechanical properties, with a decline in hardness at 820 °C compared to 650 °C. The results emphasize optimizing operational temperature and stress parameters to mitigate detrimental precipitation and cracking, thereby improving the service reliability of HIPped Astroloy components.

1. Introduction

The aerospace industry constantly strives to produce airplanes, rockets, and space shuttles with robust properties and high efficiency. To achieve these features, the industry needs materials with superior mechanical properties. For example, engine efficiency is directly related to temperature; therefore, high-temperature stable materials are required to increase the engine's temperature capabilities [1]. However, to achieve superior properties in these materials, it coexists with the difficulty of fabricating them. Moreover, a phenomenon like creep also reduces mechanical strength with long-term exposure to high temperature and stress.

Nickel superalloys are the most used materials in extreme temperature areas of aircraft due to their outstanding high-temperature properties. These alloys are employed in aircraft turbine engines operating at extreme temperatures because of their high strength, long fatigue life, and good resistance to oxidation and creep at elevated temperatures [2]. Most materials experience rapid creep at 30–40% of their melting temperature. However, Nickel superalloys resist creep so well that they can be used at approx. Up to 60-70% of their melting temperature (*T*m ~ 1280 °C) [3]. These alloys are primarily strengthened by precipitation hardening through the formation of gamma prime phase (γ'), which occurs as Ni_3(Al, Ti) compounds, mainly giving nickel super alloys long-term thermal stability and thereby providing strength and creep resistance at high temperature. In addition to precipitation hardening, a few elements, such as molybdenum and tungsten, are responsible for solid solution strengthening. Titanium, chromium, molybdenum, tantalum, niobium, and tungsten also form hard carbide precipitates: MC, $M_{23}C_6$, M_6C, and M_7C_3 by reacting with carbon (M stands for the alloying element). Each plays a distinct role by providing strength to the material by pinning, especially resistance to grain boundary sliding or embrittling the structure in the form of continuous films at grain boundaries [4]. MC carbides, typically Ti/Ta/Nb/Hf-rich, are found both in the grains and at the grain boundaries as discrete particles, providing a pinning effect that impedes grain boundary motion and provides strength to the material. In contrast, it can also decompose to $M_{23}C_6$ or $M_6C + \eta$, after prolonged or extreme exposure to high temperature, which can embrittle grain boundaries. M_6C carbides are

* Corresponding author.
E-mail address: jehanzaib.anwar@polito.it (J. Anwar).

https://doi.org/10.1016/j.jmrt.2026.03.239
Received 29 December 2025; Received in revised form 13 March 2026; Accepted 26 March 2026
Available online 31 March 2026

beneficial when discrete, pinning boundaries and improving creep resistance, while $M_{23}C_6$ (Cr-rich) carbides form continuous films on the grain boundaries and are harmful, causing intergranular embrittlement and chromium depletion [5,6]. However, these multiple elements and strengthening mechanisms significantly reduce formability, emphasizing the need for an alternative fabrication method for these high-strength materials, typically manufactured by wrought and casting routes, resulting in limited workability and mechanical properties.

Therefore, powder metallurgy can be used as an appealing alternative fabrication method to address this issue. Upon further classification, near-net-shape hot isostatic pressing (NNS–HIP) emerges as the leading option, offering a lean and efficient way to produce NNS parts using powders with a high fly-to-buy ratio [7]. NNS-HIP is a well-established technique in which temperature and isostatic pressure are applied to a pre-designed capsule filled with powder. Gas acts as the medium for transferring pressure to the capsule, facilitating the densification [8,9]. Afterward, the capsule is removed to yield the final part with minimal machining involved.

NNS-HIP has been used in the industry to consolidate different metallic powders, including nickel superalloys, to a final product shape, demonstrating properties equivalent to wrought alloys. Nickel superalloys such as Inconel 718 [10,11], Inconel 625 [12], FGH96 [13], FGH97 [14], FGH4096 [15], RR1000 [16], and CM247LC [17] have been extensively utilized due to their superior high-temperature performance. However, most of these alloys exhibit performance degradation, particularly in terms of mechanical properties above 600 °C due to the harsh working conditions, including extreme temperatures and stress for longer periods, resulting in microstructure evolution due to diffusion and dislocation movement [18,19]. In contrast, astroloy has been specifically developed to maintain a balanced combination of strength, ductility, and thermal stability beyond 600 °C, making it a more suitable choice for high-temperature aerospace applications [20]. However, optimization of its microstructure is crucial to achieve the desired optimum properties. In recent years, multiple studies have been conducted to optimize HIPping parameters to achieve the desired microstructure containing optimized grain size, precipitates, volume fraction of precipitates, and prior particle boundaries (PPBs) to achieve optimum thermomechanical properties. In this context, Blavette et al. [21] investigated the microstructure of astroloy, fabricated via HIP, revealing that its composition and cooling rate influence the microstructure, affecting grain boundary segregation, and precipitate formation influences the mechanical properties. More recently, Bassini et al. [22] optimized the effect of solution treatments on the microstructure and hardness of HIPped astroloy. It was observed that sub- and super-solvus solution treatment has an impact on γ' precipitate morphology, grain coarsening, and hardness. Results showed that higher temperatures led to increased grain size, and a decrease in precipitate size and γ/γ' ratio. Similarly, in another study, the effects of aging on HIP-processed astroloy were examined. The first aging at 760 °C for 8 h was observed to have improved the hardness significantly. While the second aging (650-675 °C) has minimal impact on hardness and introduces $M_{23}C_6$ carbides at grain boundaries, potentially reducing ductility [23].

Creep is a significant failure mode of structures operating in high-temperature environments. Considering this, many researchers have studied the relationship between microstructure evolution and creep behavior in HIPped nickel superalloys. Peng et al. [24] studied the effects of solution heat-treatment temperatures on the creep resistance of FGH96 powder metallurgy nickel-based. It was found that optimal creep resistance was achieved at 1160 °C due to balanced grain boundaries, dislocation density, and carbide presence. Similarly, J. Xie et al. [25] examined the relationship of dislocation interactions, grain boundary strength, and γ' phase morphology on creep resistance at different temperatures and stress levels in a HIPped FGH95 nickel-based superalloy. The results showed that the dislocation networks at γ/γ' interfaces relieve lattice misfit stress, thereby delaying dislocation shearing and enhancing creep resistance, while coarse γ' boundaries influence deformation mechanisms. However, only a few studies have been reported regarding the creep behavior of HIPped astroloy. Bain and Pelloux [26] investigated the effect of oxygen on creep crack growth in HIPped astroloy at 704 °C. The study revealed that oxygen accelerates the crack propagation by enhancing the grain boundary embrittlement, and the crack path shifts to the grain boundary instead of PPBs. Furthermore, it was suggested that the higher boron content is useful in the prevention of oxygen embrittlement. More recently, Bassini et al. [27] studied the microstructural evolution of HIPped astroloy after prolonged exposure to 820 °C for 200 h and reported the deteriorating effect on mechanical properties. However, the impact of creep rupture tests under different temperatures and stress conditions on microstructure and its consequence on the mechanical properties of HIPped astroloy has not been studied in detail, as per the author's best knowledge.

This work uses HIP to obtain a fully densified astroloy billet starting from pre-alloyed powders. Post-HIPping solution treatment at below the solvus temperature was performed, followed by controlled quenching to recover negative microstructural features formed due to slow cooling in the HIP equipment. Single aging is then applied for the complete heat treatment recipe. The present work deals with a study regarding the effect of creep on the HIPped astroloy. Great attention is given to how temperature and applied stress may influence the microstructure and impact the material's mechanical properties. The evolution of γ' precipitates and cracks at different creep temperatures and stress has been correlated to the mechanical properties of the material, i.e., micro-vicker hardness levels.

2. Materials and methods

2.1. Samples production

In this study, commercial astroloy powder was consolidated using the HIP to form a bar of 100 × 100 × 1000 mm^3 at 1150 °C under 103 MPa for 3h [20]. The bar was subsequently sectioned and subjected to sub-solvus heat treatment using a vacuum furnace (102 mbar), TAV MINIJET HP S/N 235, at 1115 °C with a dwell time of 4 h, followed by nitrogen quenching with a cooling rate of 70 °C/min, as discussed in detail by Bassini et al. [22]. Subsequently, single-step aging treatment was performed based on previous studies focused on the optimization of heat-treatment conditions for astroloy [20,28].

2.2. Thermal analysis

For thermal analysis, differential scanning calorimetry (DSC) was performed using Setaram thermo-analyzer labsys Evo., in which a sample weighing 181 mg was subjected to heating with a rate of 15 °C/min from room temperature to 1400 °C under argon atmosphere was carried out to understand the comprehensive picture of the critical metallurgical transformations of astroloy, including γ' precipitation/dissolution behavior, carbide evolution, and overall thermal stability, to support the interpretation of the subsequent heat treatment cycle and results.

2.3. Chemical composition

Table 1 presents the chemical composition of the bar, as determined by plasma emission spectroscopy using the SP12 model TJA Iris Advantage Radial. Carbon and sulfur were measured using the combustion infrared detection technique (Leco CS744), while oxygen and nitrogen were assessed via an inert gas fusion system (Leco TC436AR).

2.4. Mechanical testing

High-temperature creep tensile tests were performed at 650, 760, and 820 °C under varying stress conditions following ASTM E139-11.

Table 1
Alloy chemical composition.

Element	Ni	Co	Cr	Mo	Al	Ti	Fe	Zr	N	C	S	O
Wt. %	Bal.	17.8	14.3	5.62	4.6	3.68	0.18	0.05	0.004	0.014	<0.002	0.01

The applied conditions were selected to achieve measurable stress-rupture within reasonable experimental durations while maintaining conditions representative of the creep regime experienced by nickel-based superalloys in turbine service. The heat-treated sections of the NNS-HIPped sample were then machined into creep tensile samples. Nine samples were machined and tested at different temperatures and stress conditions, as shown in Table 2.

Also, Micro-hardness tests were performed using a Leica VMHT by calculating the mean of five indentations for each reading with an applied load of 500 g, and the dwell time was 15s.

2.5. Microstructural analysis

The microstructural analysis was performed on bakelite-embedded specimens, which were prepared using standard metallographic methods. This process involved sectioning, grinding, and polishing using SiC papers (100 to 2400 grit size) and velvet cloths (containing diamond and silica pastes) with particle sizes ranging from 6 to 0.1 μm. Optical micrography was performed with a metallographic microscope, Leica MEF4, on the etched sample, and the micrographs were used to evaluate creep damage and grain coarsening. Five intercepts were drawn on five different pictures for grain coarsening evaluation, and measurements were averaged as proposed in ASTM E112.

While electronic microscopy was performed with a Scanning Electron Microscope EVO 15 (SEM) with an EDS probe by Oxford Instruments Ultim max 40 (40-170 mm^2 sensor area). Samples were observed at 5, 15, and 30 KX, depending on the particles to resolve, after chemical etching using Kalling 2 solution (5 g $CuCl_2$, 100 ml HCl, and 100 ml CH_3CH_2OH) for grain boundaries and electrolytic etching by 20% H_3PO_4 at 5 V for 5-10 s to reveal γ′ precipitates morphology. For assessment, 5 pictures were processed using ImageJ open-source software, and the particle average size and percentages were evaluated for primary, secondary, tertiary γ', and carbides. Moreover, Electron backscatter diffraction (EBSD) analysis was also performed on the as-polished samples using a Tescan S9000G focused ion beam scanning electron microscope (FIB-SEM) equipped with an Oxford symmetry EBSD detector using a step size of from 0.8 to 1.5 μm, to analyze the relationship between crack propagation, grains, and grain boundaries.

3. Results

3.1. Thermal analysis of creep samples

The DSC result of the astroloy is shown in Fig. 1, where multiple metallurgical transformations occur during the heating and cooling cycles. As the temperature rises from room temperature to 1400 °C, several endothermic reactions occur during heating, while exothermic reactions occur during cooling. The first endothermic peak, occurring around 1134 °C, indicates the dissolution of the γ′ precipitates into the γ matrix, which can be regarded as the solution treatment temperature of the alloy. The total enthalpy calculated during this transformation was 39.76 J/mg, indicating the energy absorbed during the dissolution. Further heating results in the melting of the alloy, marked by a sharp endothermic peak at 1356 °C. Furthermore, multiple exothermic peaks are observed in the cooling process from 1400 °C, signaling the solidification and later precipitation behavior. The initial exothermic peaks relate to γ-phase nucleation at 1333 °C, while later exothermic reactions indicate the precipitation of multimodal γ′ particles.

Table 2
Creep samples: labels, test temperatures, and applied loads.

Sample	1	2	3	4	5	6	7	8	9
Temp (° C)	820	820	820	760	760	760	650	650	650
Load (MPa)	303	220	160	510	380	320	960	885	810

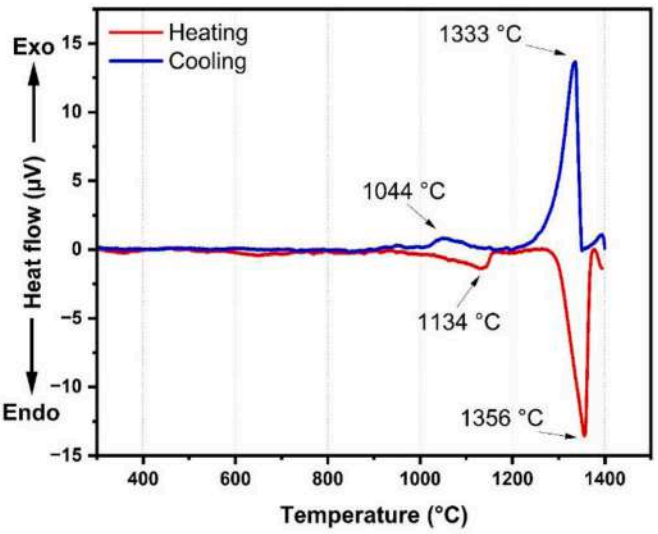

Fig. 1. DSC heating and cooling curves of astroloy with a ramp rate of 15 °C/min.

3.2. Effect of creep temperature on stress and time of fracture

To compare the creep rupture behavior of astroloy, creep data at different temperatures, i.e., 650, 760, and 820 °C, are described into a single Larson–Miller Parameter (LMP) curve (along with the approximate values of waspaloy from the literature for comparison [29]) using the following equation:

$$P = T_k\left[C + Log_{10}T_r\right] \quad (1)$$

Where P is the Larson-Miller parameter, T_k is the absolute temperature in kelvin, T_r is the rupture time in hours, and C is an empirical constant with a value of 20.

As shown in Fig. 2, all datasets follow a common linear trend, as indicated by the linear curve fit equation (2), with an R^2 value of 0.998, which suggests that 99.8% of the variance in stress versus LMP is explained.

$$\sigma_{rup} = 591.80 - 0.02268 \cdot P \quad (2)$$

Here, σ_{rup} indicates the rupture stress. The negative slope indicates that higher P (due to higher temperature or longer rupture time) corresponds to lower allowable stress. This trend reflects the temperature and time dependence of creep deformation in nickel-based superalloys, where increasing temperature accelerates diffusion-controlled processes, resulting in a decrease in rupture stress, which is consistent with the literature and the counterpart nickel-based superalloys, i.e., waspaloy [29]. However, due to industrial confidentiality associated with the collaborative project, the numerical values of the X and Y-axis in the plot are not disclosed. Nevertheless, the overall trend and comparative behavior of the creep properties are clear. Furthermore, different

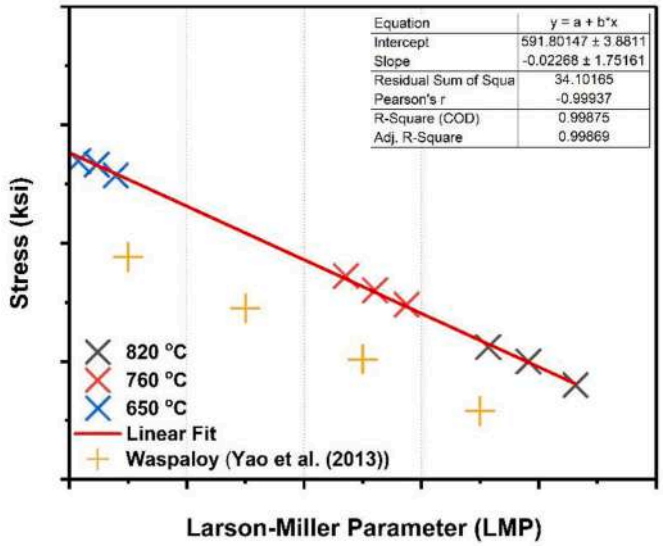

Fig. 2. Stress vs Larson–Miller parameter at 650, 760, and 820 °C of astroloy.

temperatures have different values in the graph, but they fall onto a single linear line, signifying a single creep mechanism over this range. Temperature does not change the mechanism; it only shifts the operating point along the linear line.

Moreover, using 820 °C as the reference, the percentage differences in average rupture stress were calculated for 650 °C and 760 °C. The results show that at 650 °C, the average stress required for rupture was 147.07% higher compared to 820 °C. While the difference in the average stress was 52.91% between 760 °C and 820 °C, indicating that the temperature has a significant effect on the rupture stress and time in the astroloy.

3.3. Microstructural alterations with temperature

3.3.1. Grain size and crack growth

Fig. 3 shows the optical and scanning electron micrographs of the heat-treated HIPped samples, which serve as a reference for measuring the effect of creep temperature and stress on the microstructure.

Optical microscopy was used to evaluate the damage on both the near and far surfaces of the crept samples, along with measuring the grain size at 650, 760, and 820 °C, as shown in Fig. 4. The average grain size of 33.5 ± 6.5 μm was measured near and far from the surface of the crept samples, with no clear difference in grain size as compared to the heat-treated as-built sample. As recently reported by Bassini et al. [22, 27], the grain size and shape didn't change after prolonged exposure to high temperatures, as the grain size depends on the solution treatment temperature during heat treatment in astroloy. It increases with the increase in solution treatment temperature and vice versa. As the heat treatment process is the same for all the crept samples, it can be concluded that the creep temperature doesn't affect the grain size. Furthermore, intergranular macro cracks are visible on the near-surface but not present on the far-surface images, as creep is more prominent on the near-fracture surface. A similar effect of temperature was observed as the temperature decreased below 760 °C, with a sharp decline in defects, including cracks and creep cavities, evident in the images. Specifically, the average crack length increased from 13.23 to 36.44 μm as the temperature increased from 650 to 760 °C and further to 69.24 μm at 820 °C. Likewise, the percentage porosity also shows the same trend near the fracture surface, increasing from 0.0098% to 0.036% and 0.197% with temperature, respectively. However, stress conditions don't show any significant change in the microstructure, indicating that temperature is the major element influencing the microstructure. Moreover, the direction of the cracks perpendicular to the direction of the force along the grain boundary was observed due to the grain boundary sliding at high temperatures [30]. Also, twin boundaries identified by their characteristic sharp linear features and PPBs are visible in optical images, marked by white circles and arrows pointing toward the PPBs. Twin boundaries provide additional strength to the material by impeding dislocation motion more efficiently than grain boundaries due to their low interfacial energy [31], while PPBs deteriorate the properties by providing crack initiation and propagation sites [32].

To further analyze the crack initiation and growth mechanisms, EBSD was performed. EBSD analysis after creep testing at 650 °C, 760 °C, and 820 °C, along the direction of the applied load, is shown in Fig. 5. Each temperature condition is represented by four maps: an inverse pole figure (IPF) map, a band-contrast (BC) map, kernel average misorientation (KAM) map and a grain reference orientation deviation (GROD) map.

At 650 °C (Fig. 5a–d), the microstructure shows equiaxed grains with an intergranular crack propagating along a grain boundary. The KAM map reveals that the green area, indicating local misorientation caused by local strain or dislocations, extends across both the grain boundary and the interior. The Σ3 fraction is approximately 34%, indicating a twin-rich and relatively stable boundary network. In contrast, a high percentage (approx. 89%) of high-angle grain boundaries (HAGBs, >10°) was measured, whereas low-angle boundaries (LAGBs, 2°–10°) are only 10 %. When the creep temperature increases to 760 °C and 820 °C, the micrograph becomes more deteriorated. The KAM and GROD maps clearly show a change in pattern as misorientation zones form along grain boundaries, leading to increased cracks and voids,

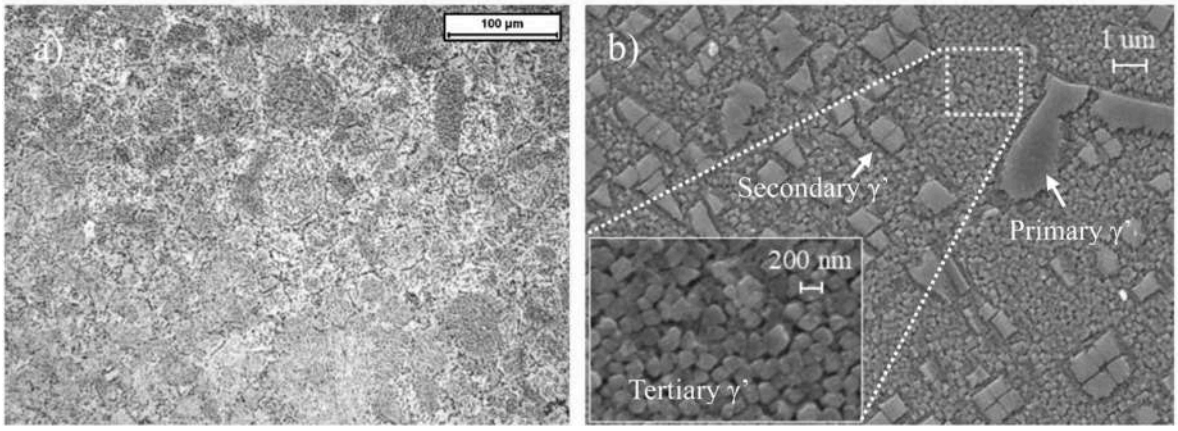

Fig. 3. Microstructure of heat-treated as HIPped astroloy a) 200X b)15KX.

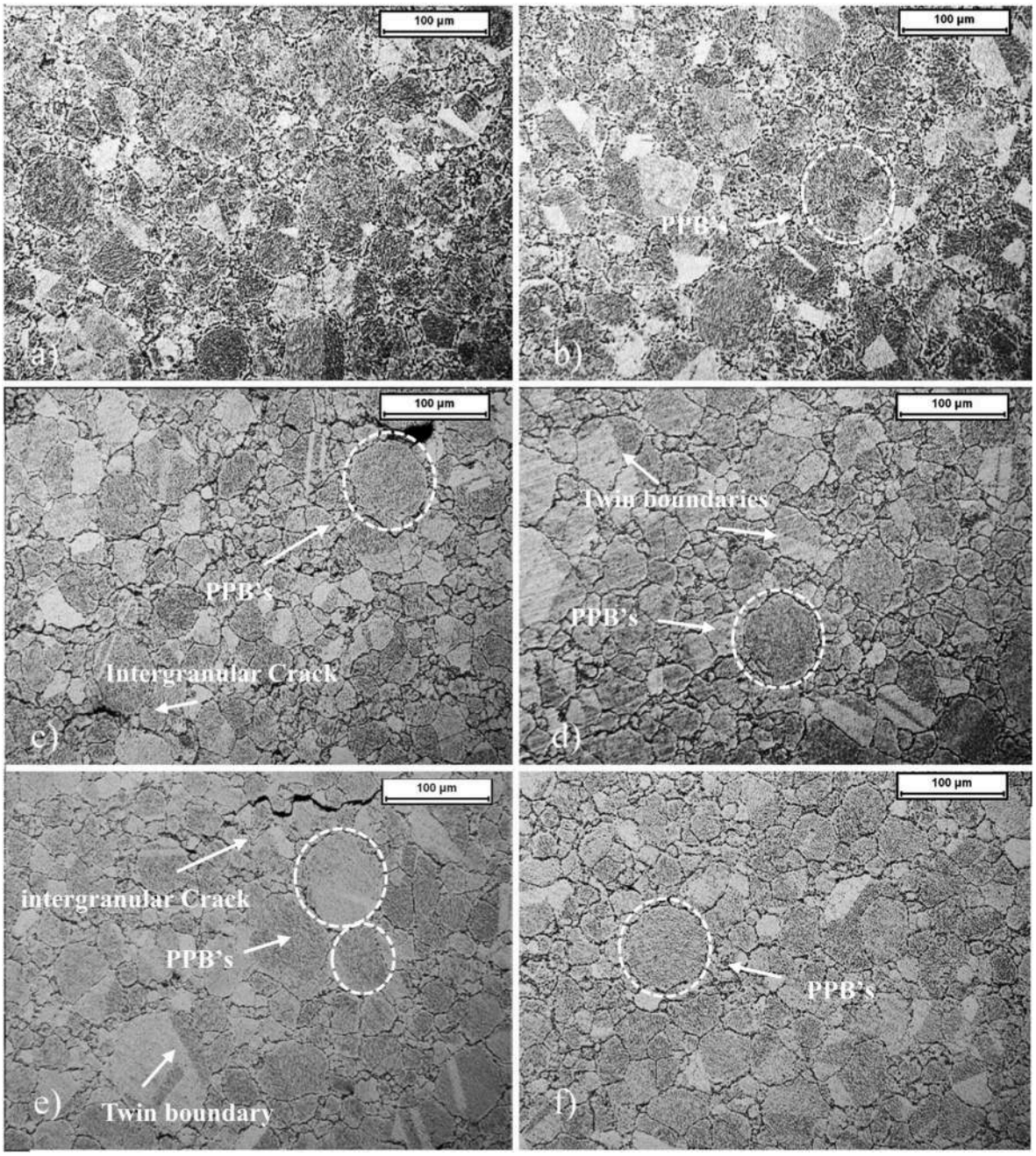

Fig. 4. Optical images of crept samples near (~100 μm) and far (~3 mm) surface (a) & (b) at 650 °C, (c) & (d) at 760 °C, and (e) & (f) at 820 °C. All samples were etched with Kalling 2 solution.

while the grain interiors appear less strained. This suggests that plastic strain becomes concentrated at the boundaries rather than spread throughout the grain. The Σ3 percentage drops slightly to 33% and 30%, respectively. The slight decrease in Σ3 boundary fraction with increasing temperature is within the expected EBSD scatter and is consistent with reports that these boundaries can be partially annihilated/consumed by migration during high-temperature exposure [33].

3.3.2. Evolution of gamma prime precipitates

Similarly, electron microscopy revealed the microstructure at 5, 15, and 30 KX magnification, consisting of a gamma matrix with multiple types of reinforcing particles (γ′) – Ni_3(Al, Ti), varying in size and shape. Based on the different sizes and shapes in the microstructure of the heat-treated HIPped sample, as shown in Fig. 3b, they are classified into three types, i.e., primary, secondary, and tertiary. Primary γ′ is the largest precipitate present on the grain boundaries with an average size of 2.63 ± 0.9 μm and an elliptical shape. Secondary and tertiary precipitates have an average size of 0.60 ± 0.12 μm and 0.16 ± 0.03 μm, respectively, with a cuboidal shape. Furthermore, a fourth type of nano-sized particles is also present, which coalesce to form larger particles [18,27] or coarsen as the temperature increases [27,34]. Together with γ', a small amount of loose and round Molybdenum carbides are also detected on the grain boundaries as well as in the grains and will be discussed in the next section in detail.

However, as the temperature increases, the size, shape, and concentration of the precipitates change. Fig. 6 compares the microstructure of creep samples at different temperatures. The pictures show that as the temperature increases, it results in the coarsening behavior of tertiary γ′, which is also accompanied by an increase in the volume fraction. It is also observed that the ternary γ′ size increases by 18%, precisely, on

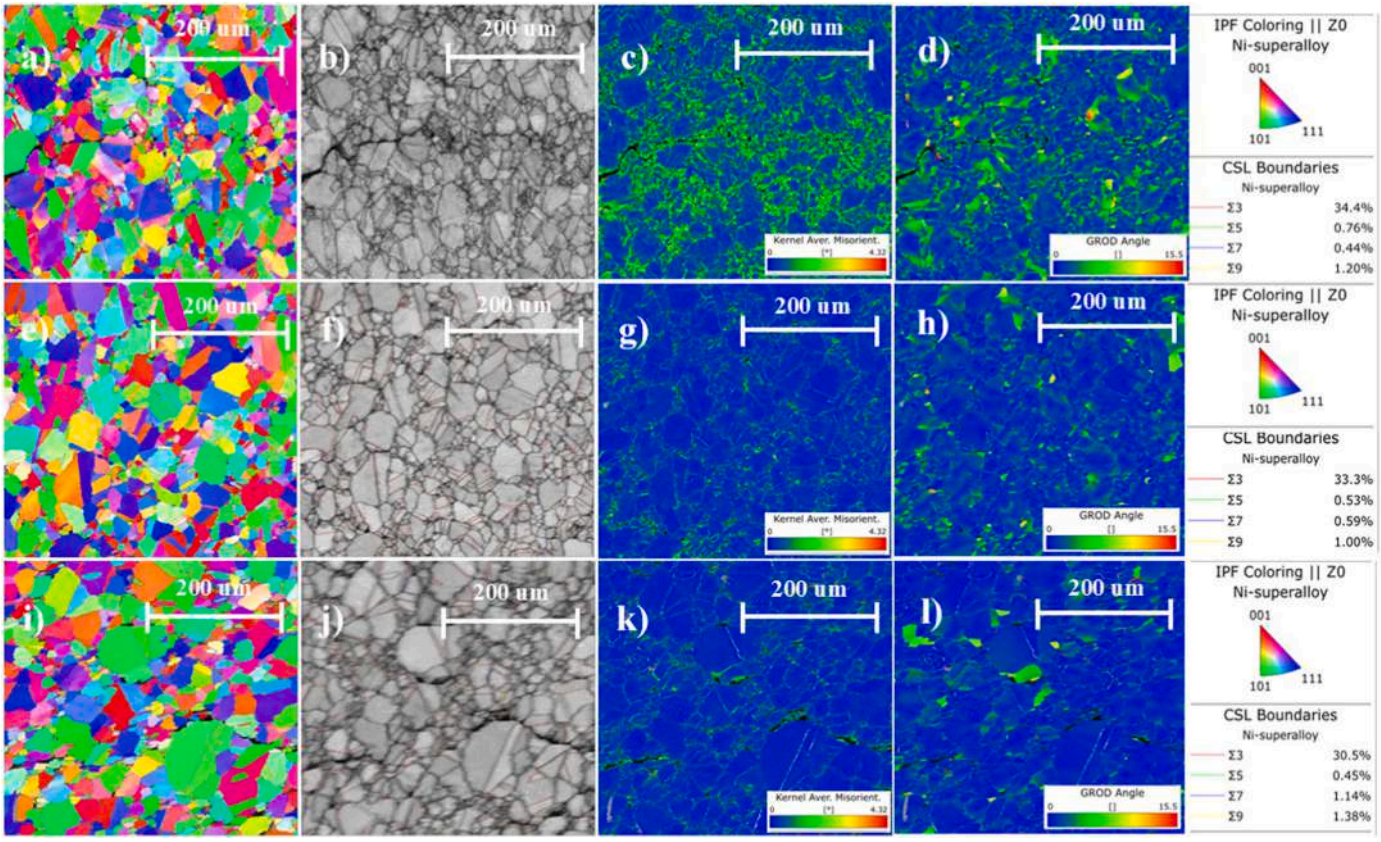

Fig. 5. EBSD analysis of specimens crept at (a–d) 650 °C, (a) inverse pole figure (IPF) map, (b) BC map, (c) KAM map, (d) GROD map; (e–h) 760 °C; and (i–l) 820 °C.

average, from 150 ± 25 to 210 ± 33 nm in the creep samples at 760 and 820 °C, as illustrated in Fig. 7. Furthermore, this ternary γ′ lost its original cuboidal shape and became spherical. Moreover, the overall percentage of γ' increases from 37% to 46% with the temperature increase from 650 °C to 820 °C.

Apart from changes in the size and shape of precipitates, micro and macro cracks are also observed due to grain boundary sliding. Only a few cracks are observed near the fracture surface at 650 °C. However, increasing the temperature from 650 °C to 820 °C increased the percentage of cracks and changed from micro to macro. Similarly, the percentage of cracks decreases with the increase in distance from the fracture surface.

3.3.3. Carbide transformation

Like γ', spherical-shaped carbides are present in the astroloy and observed both in the grains and on the grain boundaries of the microstructure of the HT HIPped samples with an average diameter of 1.1 μm and a volume fraction of 0.37 %. However, they are more clearly visible in spherical shape, in the backscattered mode in SEM, as shown in Fig. 8, due to the difference in atomic number between the carbides and the surrounding matrix/precipitates, resulting in compositional contrast. However, as the creep temperature is increased, the evolution of carbides is observed as illustrated in Fig. 9. At 650 °C, the carbides are spherical with an average diameter and a volume fraction approximately the same as that of the reference sample. As the temperature increases to 760 and 820 °C, the carbide percentages significantly increase to 2.81% and 3.60%. However, the percentage of round carbides remains approximately the same; the increase in the overall percentage was due to the formation of elongated carbides along the grain boundaries. On further analysis through EDS, it was observed that spherical carbides are rich in Mo and can be referred to as M_6C carbides, as reported in the literature. However, the elongated and irregular carbides along the grain boundaries are rich in Cr, Compliant with the $M_{23}C_6$ family, recognizable for the elongated shape and the nucleation site [4], resulting in the formation of semi-continuous and continuous film, providing a preferential path for the crack to grow, and resulting in crack formation. Moreover, differences in brightness can also be observed in the micrographs between the two different types of carbides due to differences in composition; M_6C appeared brighter than $M_{23}C_6$ due to a higher atomic number of Mo than Cr.

3.4. Effect of creep temperature on hardness

Various studies have confirmed the effects of microstructure, i.e., precipitate size and volume fraction, on the mechanical properties of nickel superalloys. The micro-vickers hardness test evidenced a general softening in nickel superalloys from 650 °C to 820 °C. More specifically, the hardness level decreases by approximately 24% on average. On further examination, it was observed that the decrease in hardness is due to the precipitation coarsening and coalescence, while carbide precipitation results in an increase in hardness. Similarly, Wang et al. [35] also reported ~5-6% loss in hardness during air-cooling and furnace cooling of MAR-M247, due to γ′ coarsening and morphology evolution. However, the significant decrease in the hardness was due to the microcracks and voids present on the grain boundaries. When the force is applied by the indenter near the surface, the already present microcracks and voids grow and propagate along the grain boundaries, as shown in Fig. 10.

As the number of cracks along with microstructural changes, near the surface, is higher and decreases while moving away from the fracture due to a less deteriorated zone, the value of hardness increases. Fig. 11 shows the hardness versus distance from the fracture surface graph at different temperatures.

4. Discussion

This discussion first interprets the creep behavior through the

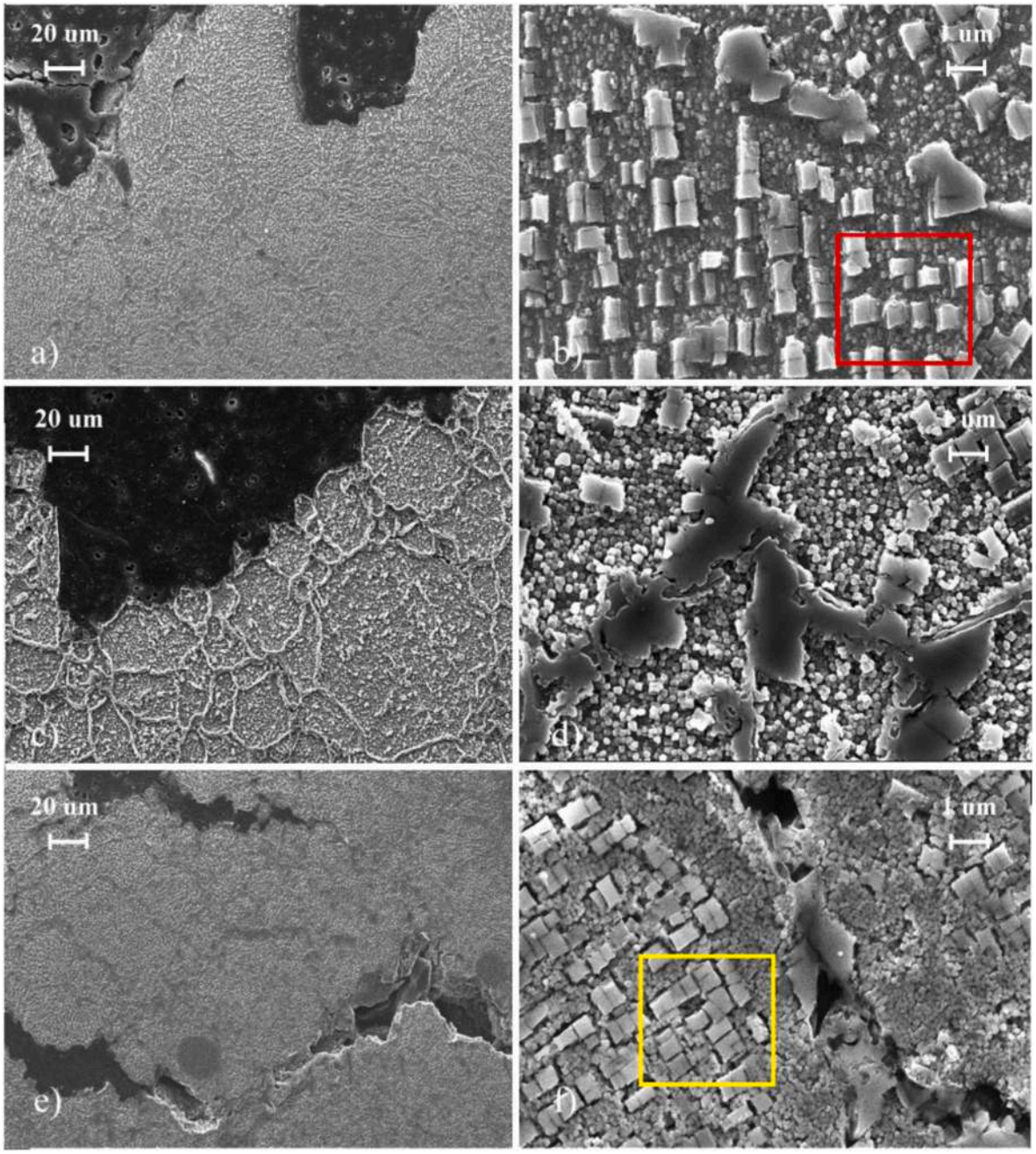

Fig. 6. SEM images of crept samples (a) & (b) at 650 °C, (c) & (d) at 760 °C, and (e) & (f) at 820 °C. All samples were electrolytically etched with 20% H_3PO_4.

Larson–Miller relationship, followed by the analysis of microstructural evolution during creep, including γ′ precipitate coarsening, carbide transformation, and deformation mechanisms revealed by EBSD. The selection of appropriate HIPping parameters results in a dense and defect-free NNS-HIPped micro-structure, a characteristic feature of the HIPping process [36]. Following HIP consolidation, sub-solvus heat treatment was performed with quenching and ageing, resulting in primary γ′ precipitates on the grain boundaries and fine precipitates of secondary and tertiary γ' within the grains. The astroloy is primarily strengthened by precipitation hardening by the formation of multimodal precipitates (37%), i.e., Ni_3(Al, Ti). These precipitates are formed due to the presence of 3-5 % of Al and Ti, as shown in Table 1. Moreover, carbides mainly on the grain boundaries provide additional creep resistance to the material by resisting the grain boundary sliding [37].

Based on the optimized microstructure, the NNS-HIPped astroloy showed better creep properties as depicted in stress vs LMP in Fig. 2, compared to its counterpart. The stress vs LMP plot also describes the combined relationship of rupture stress, temperature, and time on the creep behavior of the alloy. The graph shows that at lower temperatures, i.e., 650 °C, the material takes comparatively more time to rupture due to slower atomic diffusion and reduced grain boundary damage mechanisms. However, increasing the temperature to 760 °C and 820 °C significantly reduces rupture time, ultimately reflected by a decrease in the LMP values. This behavior can be attributed to accelerated diffusion, which causes γ′ precipitate coarsening, carbide precipitation along grain boundaries, and grain boundary sliding, as also evident from the optical and SEM micrographs. This correlation between rupture stress, time, and microstructural degradation confirms that temperature strongly influences creep damage accumulation in HIPped astroloy.

To further understand the microstructural evolution responsible for this reduction in creep strength, microstructural characterization was performed using optical and electron microscopy. Optical microscopy

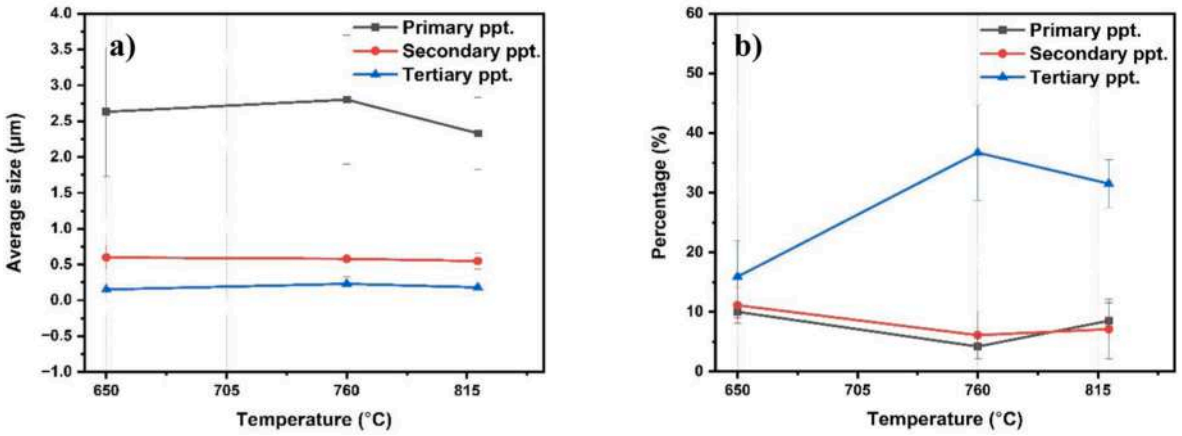

Fig. 7. a) Average precipitate sizes; b) Percentage fractions of primary, secondary, and tertiary γ′ in creep samples at 650, 760, and 820 °C.

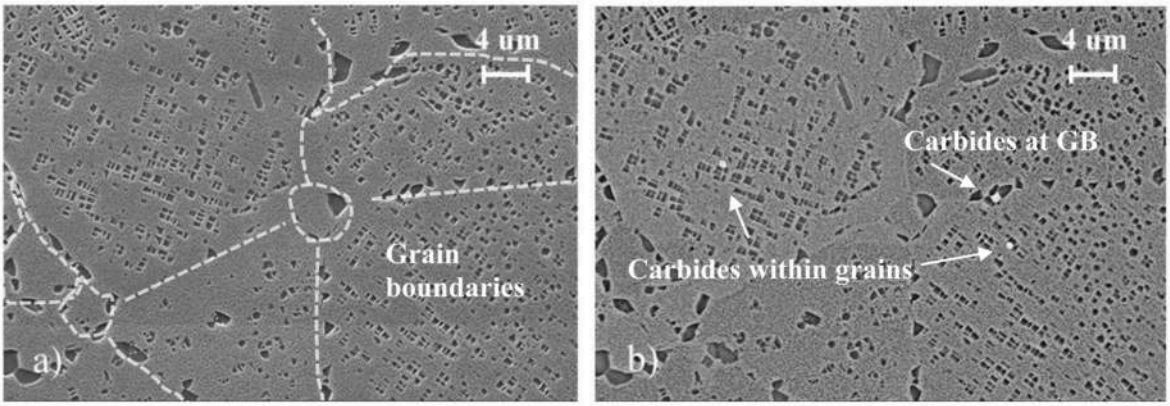

Fig. 8. SEM images of the HT HIPped sample in a) Secondary electron mode, (b) Backscattered electron mode.

was used to evaluate the deterioration and grain morphology of the creep-tested samples. Interestingly, it was observed that neither temperature nor stress affected the final grain size of the samples. This is due to the high-temperature stability of the primary and secondary precipitates, which results in precipitation hardening and hinders dislocation movement and grain boundary sliding. Furthermore, molybdenum has low atomic diffusion rates in nickel and moves very slowly through the lattice structure at these temperatures, preventing grain coarsening and resulting in increased creep resistance [3]. Grain size has a huge impact on the creep strength of the material. Larger grain size results in fewer grain boundaries, and dislocation is required to propagate to a larger distance to reach the grain boundary, resulting in increased creep resistance and vice versa [34]. Therefore, the parameters during heat treatment must be optimized depending on the application. Bassini et al. [22] observed that the grain size depends on the solution treatment temperature during HIPping in an astroloy. The grain size of the alloy increases with the increase in the solution treatment temperature. Therefore, careful selection of the heat treatment process is very important based on the intended application. Moreover, equiaxed grains were observed in the optical images, with the cracks visible perpendicular to the applied stress direction.

Similarly, Electron microscopy revealed the changes in the microstructure at the micron level as the temperature increased from 650 °C to 820 °C, as compared to the HT HIPped samples, as illustrated in Fig. 12. It was observed that the tertiary γ′ experiences the most prominent changes in shape, size, and concentration, while the primary and secondary γ′ remain unaffected except for joining at a few points, as also indicated by the red and yellow areas in Fig. 6. This coarsening of tertiary γ′ precipitates during creep or long-term high-temperature exposure is due to the high surface energy of small precipitates, which, upon heating at elevated temperature, try to minimize interfacial and lattice misfit energy, facilitated by increased atomic diffusion. The same coarsening effect of tertiary γ′ due to exposure to elevated temperature has been reported in multiple studies for different nickel-based super alloys [38,39]. This results in an overall increase in γ′ percentages from 37% to 46%. This prominent increase in γ′ percentage of samples might be due to the growth of nano-sized (Quaternary) γ′ particles to form tertiary γ′, together with the coarsening of existing tertiary γ′ particles. This coarsening of γ' may happen at the expense of the smaller γ′ precipitates that dissolve, supplying solute atoms that contribute to the growth of larger particles, consistent with the classical Ostwald ripening mechanism [40].

In addition to γ′ precipitates, carbide evolution also plays an important role in the creep response of astroloy during high-temperature exposure. At elevated temperatures, thermodynamics favors the formation of carbides that are richer in elements like Cr or Mo because they lower the system's Gibbs free energy. This causes Ti in MC carbides to get replaced during long-term exposure to form secondary carbides, i.e., M_6C, $M_{23}C_6$, etc [41]. Moreover, Sun et al. [42] explained that the (W + Mo)/Cr ratio in nickel super alloys mainly controls the conversion of MC to M_6C and $M_{23}C_6$. According to the astroloy used in this study, it should have both $M_{23}C_6$ and M_6C carbides, even exposing them to higher temperatures as seen in the microstructure. Reactions associated with carbide changing the phase from MC to $M_{23}C_6$, M_6C can be described as follows [4,43]:

$$MC + \gamma \rightarrow M_6C + \gamma' \quad (3)$$

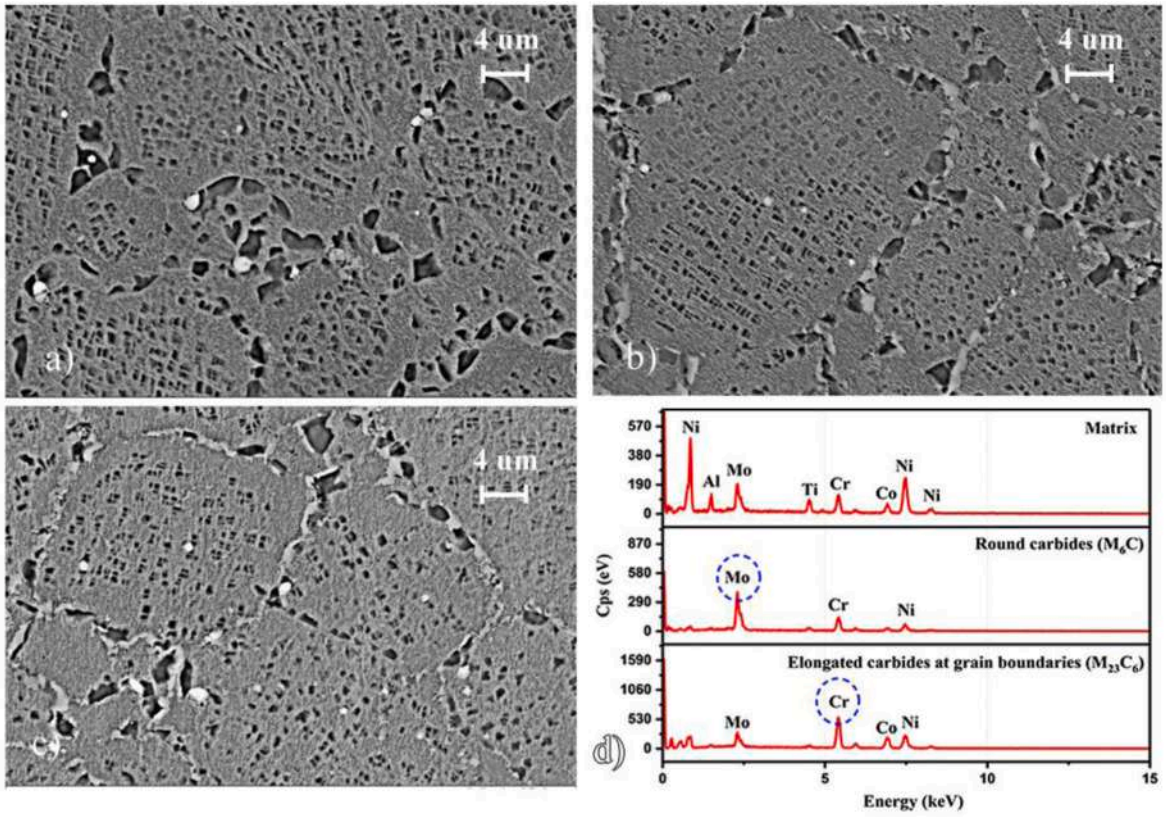

Fig. 9. BSE SEM images of Crept sample (a) at 650 °C,(b) 760 °C,(c) 820 °C, (d) EDS analysis of γ, Round carbides, and elongated carbides at grain boundaries.

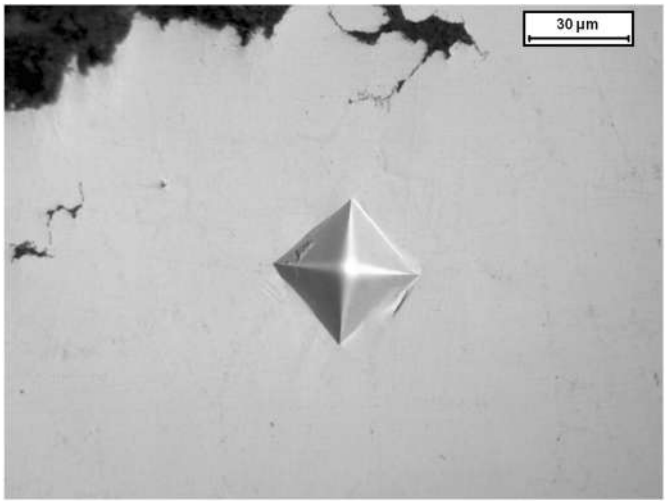

Fig. 10. Micro vicker indent on the sample crept at 760 °C.

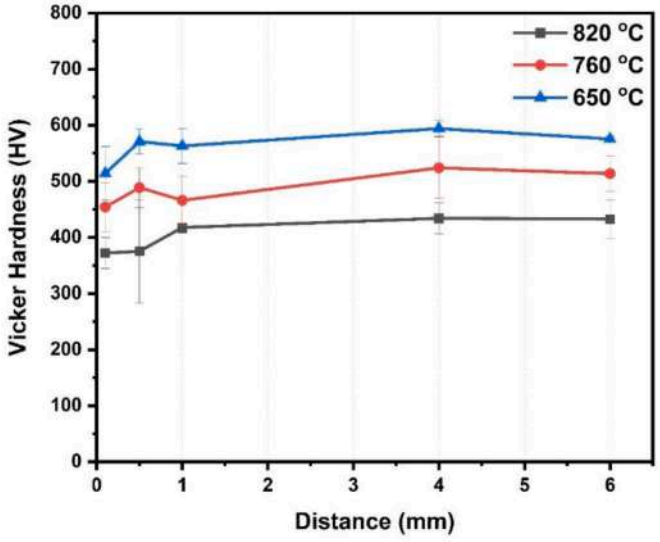

Fig. 11. Hardness vs distance from the fracture surface.

$$M_6C + \gamma \rightarrow M_{23}C_6 + \gamma' \quad (4)$$

Although M_6C carbides could transform into $M_{23}C_6$, their volume fraction remained nearly unchanged during the creep test at 760 and 820 °C. This is attributed to the predominance of new grain-boundary precipitation of Cr-rich $M_{23}C_6$ from the γ matrix, rather than decomposition of the Mo-rich M_6C. This phenomenon was only observed at higher temperatures, i.e., 760 and 820 °C, due to the faster diffusion of Cr in the γ matrix, which promotes the precipitation of grain-boundary $M_{23}C_6$. Furthermore, these continuous precipitations will result in the brittleness along the grain boundaries and can provide a preferential growth path to cracks.

To further understand the deformation mechanisms, EBSD analysis was performed, which correlates microstructural evolution with dislocation distribution and crack behavior. As shown in Fig. 5, the KAM and GROD maps reveal a temperature-dependent redistribution of dislocations. At 650 °C, large yellow regions across grain interiors indicate that dislocations are broadly distributed within the grains as the low temperature and high applied stress restrict dislocation climb and annihilation, leading to lattice curvature inside grains. At higher temperatures (760 °C and 820 °C), the intragranular KAM and GROD intensities decrease and are localized along the grain boundary due to continuous

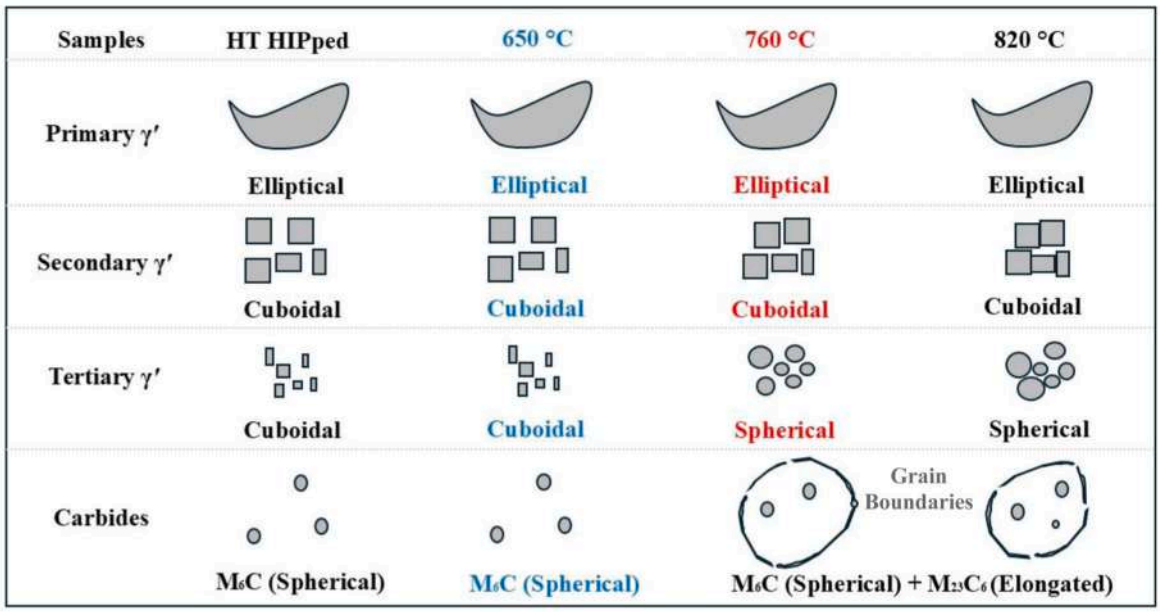

Fig. 12. Schematic illustration of the evolution of primary, secondary, tertiary γ′ precipitates and carbides in crept astroloy at 650,760, and 820 °C.

$M_{23}C_6$ films, causing strain localization. Consequently, deformation transitions from matrix to grain boundary, accompanied by grain-boundary sliding and crack nucleation. The EBSD data also confirm that cracks preferentially propagate along HAGBs due to their higher energy and carbide decoration. In contrast, LAGBs and Σ3 lattice boundaries resist propagation owing to stronger lattice continuity [44].

Furthermore, cracks are mostly seen near orientations close to {101}. As astroloy has an FCC structure in which plastic deformation mainly occurs through ⟨110⟩ dislocation glide on {111} planes. However, grains oriented at {101} relative to the loading axis may be less favorably aligned for activating these slip systems, resulting in limited slip and poor stress relaxation. Therefore, this results in misoriented grains, giving rise to cavitation and intergranular cracks. Similar behavior has been reported by Long et al. [45], explaining that the [001] orientations in directionally solidified Ni-based superalloys activate fewer slip systems, causing anisotropic creep resistance and early fracture along interdendritic or boundary regions.

Overall, the results indicate that creep cracks initiate and propagate along HAGBs with high probability at {101} due to large lattice mismatch and strain incompatibility. The high energy of these boundaries also facilitates the precipitation of $M_{23}C_6$ carbides [6], further increasing local stress concentration and enhancing intergranular crack propagation.

Moreover, the hardness test evidenced a decrease in hardness with the increased temperature and moving towards the fracture surface. The reduction in the hardness is due to the following reasons: the change in concentration, size, shape, and distribution of tertiary gamma prime. As observed in the microstructure of the creeped sample at 650 °C, the primary, secondary, and tertiary γ′ phases are separately distributed all over the microstructure. Conversely, when the temperature is increased to 760 °C and above, the coarsening of tertiary precipitates and coalescence between primary, secondary, and tertiary precipitates result in a reduced pinning effect of dislocations in the matrix. Moreover, continuous precipitates formed at higher temperatures along the grain boundaries also provide a crack propagation path, reducing the alloy's ductility. The combined effect of these factors reduces the hardness, because the increase in carbide percentage also increases hardness, nullifying the effect of precipitate coarsening, as reported by multiple researchers that the hardness values of carbides are greater than the precipitates in the nickel alloys using nano indentation techniques [46,47].

Moreover, another major reason for the significant decrease in hardness is the presence of micro and macro cracks formed due to the creep along the grain boundaries. As the distance from the fracture surface increases, both the percentage of cracks decreases, resulting in the regaining of strength. Therefore, the near-surface hardness is comparatively less than the far-surface hardness. Likewise, for the highest temperature and stress sample, the difference in near and far hardness is only 0.3 %. This is because the effect of deterioration was the same near and far from the surface, and microcracks were also observed in far areas.

Based on the above observations, it can be concluded that temperatures below 760 °C are ideal for the astroloy to function without significant changes in microstructure, resulting in sustained mechanical properties [48]. As the secondary and tertiary γ′ are the main source of strengthening in the nickel superalloy, which are also minimally affected below 760 °C. Furthermore, no signs of γ' rafting were observed in the microstructure, which is a common deterioration of the microstructure due to creep [49,50]. Therefore, astroloy can be used safely up to 760 °C, keeping the creep considerations.

5. Conclusion

Astroloy is commonly designed for use in high-temperature aerospace parts where high temperature and stress are applied to the material, resulting in creep. Therefore, the degradation of mechanical properties at multiple temperatures and stresses was analyzed due to changes in the microstructure of the material. Thus, by comparing the mechanical properties and microstructure of the creep samples at different temperatures and stress conditions, the following conclusions may be drawn:

1. The microstructural observations indicate that temperature plays a more dominant role in the evolution of microstructure as compared to stress conditions, resulting in mechanical degradation during the creep test.
2. As the temperature increases, the tertiary γ′ coarsens (18%), and the shape is changed from cuboidal to spherical. However, no significant change in primary and secondary γ′ was observed.

3. An increase in γ′ precipitates was observed from 37% to 46% and carbides from 0.37 % to 3.6 % as the temperature increased from 650 to 820 °C, forming a continuous layer along the grain boundaries, providing a path to crack formation and propagation.
4. Creep rupture stress and time decrease with increasing temperature, in compliance with the microstructural degradation at elevated temperatures observed. Consequently, the rupture stress was 147.07% higher at 650 °C and 52.91% higher at 760 °C compared to 820 °C.
5. Hardness decreases by up to 24 % as the temperature increases due to γ′ coarsening, carbide precipitation, shape change of tertiary γ′, and the presence of creep voids and microcracks at the grain boundary.

Very few cracks were observed in the samples crept at 650 °C, which increased at and above 760 °C along with the change in microstructure, i.e., ppt size, shape, and volume fraction. This indicates below 760 °C as the ideal temperature for the astroloy to be used without prominent changes in the microstructure. However, thermal analysis and hardness tests confirmed the stability even above 760 °C up to the solution treatment temperature, keeping the note on time and stress. Therefore, the HIPped fabricated astroloy can be used as a substitute for other nickel-based super alloys for better efficiency and performance. Moreover, rejuvenation heat treatments can be effectively applied to restore mechanical properties after a certain period, accurately assessing deterioration, lifespan, and economics of the part, which is missing from the literature and should be explored specifically for HIPped astroloy in future studies for an industrial perspective.

Declaration of competing interest

The authors declare the following financial interests/personal relationships which may be considered as potential competing interests: Jehanzaib anwar reports financial support was provided by European Union. If there are other authors, they declare that they have no known competing financial interests or personal relationships that could have appeared to influence the work reported in this paper.

Data availability

Data will be made available on request.

References

[1] Rolls Royce p. The jet engine. John Wiley & Sons; 2015. https://doi.org/10.1002/0471743984.vse4356.
[2] Gudivada G, Pandey AK. Recent developments in nickel-based superalloys for gas turbine applications. J Alloys Compd 2023;963:171128. https://doi.org/10.1016/j.jallcom.2023.171128.
[3] Mouritz AP. Introduction to aerospace materials. Woodhead Publishing Limited; 2012. https://doi.org/10.1533/9780857095152.
[4] Cai H, et al. The evolution of carbides during long-term creep/aging of nickel based superalloy K444. J Mater Res Technol 2024;28:3631–40. https://doi.org/10.1016/j.jmrt.2023.12.236.
[5] Yang Y, et al. Synergistic evolution of MC/M23C6 carbides in a polycrystalline Ni-based superalloy during long-term aging: elemental diffusion and interaction mechanisms. Mater Char 2025:115462. https://doi.org/10.1016/j.matchar.2025.115462.
[6] Hu R, et al. Precipitation behavior of grain boundary M23C6 and its effect on tensile properties of Ni–Cr–W based superalloy. Mater Sci Eng, A 2012;548:83–8. https://doi.org/10.1016/j.msea.2012.03.092.
[7] Sergi A. Hot isostatic pressing of high temperature materials. University of Birmingham; 2022.
[8] Aghayar Y, et al. Hot isostatic pressing of additively manufactured metallic components: a critical review on microstructure, mechanical, and corrosion properties. J Mater Res Technol 2026. https://doi.org/10.1016/j.jmrt.2025.12.306.
[9] Aghayar Y, et al. Ambient and high-temperature rotating bending fatigue of as-built and hot isostatic pressed additively manufactured 316L stainless steel. Int J Fatig 2025:109365. https://doi.org/10.1016/j.ijfatigue.2025.109365.
[10] Buckingham R, et al. The effect of strain distribution on microstructural developments during forging in a newly developed nickel base superalloy. Mater Sci Eng, A 2016;654:317–28. https://doi.org/10.1016/j.msea.2015.12.042.
[11] Rao GA, et al. Effect of standard heat treatment on the microstructure and mechanical properties of hot isostatically pressed superalloy inconel 718. Mater Sci Eng, A 2003;355(1-2):114–25. https://doi.org/10.1016/S0921-5093(03)00079-0.
[12] Wang JW, et al. Study on direct hot isostatic pressing technology for superalloy inconel 625. Adv Mater Res 2011;189:2935–8. https://doi.org/10.4028/www.scientific.net/AMR.189-193.2935.
[13] Nie L, et al. Constitutive modeling of dynamic recrystallization kinetics and processing maps of solution and aging FGH96 superalloy. J Mater Eng Perform 2013;22:3728–34. https://doi.org/10.1007/s11665-013-0699-4.
[14] Qu Z, et al. Influence of powder particle size on the microstructure of a hot isostatically pressed superalloy. J Mater Res Technol 2022;16:1283–92. https://doi.org/10.1016/j.jmrt.2021.12.081.
[15] Ning Y, Fu M, Yao W. Recrystallization of the hot isostatic pressed nickel-base superalloy FGH4096. II: characterization and application. Mater Sci Eng, A 2012;539:101–6. https://doi.org/10.1016/j.msea.2012.01.065.
[16] Qiu C, et al. Influence of heat treatment on microstructure and tensile behavior of a hot isostatically pressed nickel-based superalloy. J Alloys Compd 2013;578:454–64. https://doi.org/10.1016/j.jallcom.2013.06.045.
[17] Zhang Q. The microstructure and properties of powder HIPped nickel-based superalloy CM247LC. University of Birmingham; 2011.
[18] Ali MA, et al. Effect of γ′ precipitate size on hardness and creep properties of Ni-base single crystal superalloys: experiment and simulation. Materialia 2020;12:100692. https://doi.org/10.1016/j.mtla.2020.100692.
[19] Roy AK, Venkatesh A. Evaluation of yield strength anomaly of alloy 718 at 700–800° C. J Alloys Compd 2010;496(1-2):393–8. https://doi.org/10.1016/j.jallcom.2010.02.023.
[20] Raisson G, et al. Production of net-shape static parts by direct HIPing of nickel base superalloy prealloyed powders. Adv Mater Res 2011;278:277–82. https://doi.org/10.4028/www.scientific.net/AMR.278.277.
[21] Blavette D, et al. Atomic-scale APFIM and TEM investigation of grain boundary microchemistry in astroloy nickel base superalloys. Acta Mater 1996;44(12):4995–5005. https://doi.org/10.1016/S1359-6454(96)00087-0.
[22] Bassini E, et al. Influence of solutioning on microstructure and hardness of hot isostatically pressed astroloy. J Alloys Compd 2017;723:1082–90. https://doi.org/10.1016/j.jallcom.2017.06.332.
[23] Bassini E, et al. Study of the effects of aging treatment on astroloy processed via hot isostatic pressing. Materials 2019;12(9):1517. https://doi.org/10.3390/ma12091517.
[24] Peng Z, et al. Effects of solution temperatures on creep resistance in a powder metallurgy nickel-based superalloy. Mater Today Commun 2021;28:102573. https://doi.org/10.1016/j.mtcomm.2021.102573.
[25] Xie J, et al. Creep behaviors and role of dislocation network in a powder metallurgy Ni-based superalloy during medium-temperature. Mater Sci Eng, A 2014;606:304–12. https://doi.org/10.1016/j.msea.2014.03.088.
[26] Bain KR, Pelloux RM. Effect of oxygen on creep crack growth in PM/HIP nickel-base superalloys. Superalloys 1984:387–96. https://doi.org/10.7449/1984/superalloys_1984_387_396. 1984.
[27] Bassini E, et al. Assessment of the reinforcing system and carbides evolution in hot isostatically pressed astroloy after prolonged exposure at 820 C. Mater Sci Eng, A 2020;773:138879. https://doi.org/10.1016/j.msea.2019.138879.
[28] Raisson G. Evolution of PM nickel base superalloy processes and products. Powder Metall 2008;51(1):10–3. https://doi.org/10.1179/174329008X286631.
[29] Yao Z, Zhang M, Dong J. Stress rupture fracture model and microstructure evolution for Waspaloy. Metall Mater Trans 2013;44(7):3084–98.
[30] James A. Review of rejuvenation process for nickel base superalloys. Mater Sci Technol 2001;17(5):481–6. https://doi.org/10.1179/026708301101510168.
[31] Zhang Z, et al. Strain localisation and failure at twin-boundary complexions in nickel-based superalloys. Nat Commun 2020;11(1):4890. https://doi.org/10.1038/s41467-020-18641-z.
[32] Galech U, et al. Effect of astroloy powder characteristics on mechanical properties of Powder-HIP components. Mater Sci Eng, A 2024;900:146472. https://doi.org/10.1016/j.msea.2024.146472.
[33] Chen X-M, Lin Y, Wu F. EBSD study of grain growth behavior and annealing twin evolution after full recrystallization in a nickel-based superalloy. J Alloys Compd 2017;724:198–207. https://doi.org/10.1016/j.jallcom.2017.07.027.
[34] Thibault K, et al. Influence of microstructure on local intra-and intergranular deformations during creep of a nickel-based superalloy at 700 C. Mater Sci Eng, A 2013;588:14–21. https://doi.org/10.1016/j.msea.2013.09.015.
[35] Wang Y, et al. Effect of cooling rate on the microstructure and mechanical property of nickel-based superalloy MAR-M247. Materials 2024;17(5):982. https://doi.org/10.3390/ma17050982.
[36] Aghayar Y, et al. Tailoring the microstructure, physical, and mechanical properties of pure copper using various additive manufacturing techniques. J Alloys Compd 2025;1010:178332. https://doi.org/10.1016/j.jallcom.2024.178332.
[37] Dong X, et al. Microstructure of carbides at grain boundaries in nickel based superalloys. J Mater Sci Technol 2012;28(11):1031–8. https://doi.org/10.1016/S1005-0302(12)60169-8.
[38] Wangyao P, et al. Gamma prime particle coarsening behavior at elevated temperatures in cast nickel-based superalloy, GTD-111 EA. High Temp Mater Process 2008;27(1):41–50. https://doi.org/10.1515/HTMP.2008.27.1.41.
[39] Zhang F, et al. Microstructural stability and mechanical properties of GH742 Ni-based wrought superalloy for turbine disk applications. Mater Sci Eng, A 2022;832:142488. https://doi.org/10.1016/j.msea.2021.142488.
[40] Bian H, et al. Regulating the coarsening of the γ′ phase in superalloys. NPG Asia Mater 2015;7(8):e212. https://doi.org/10.1038/am.2015.96. e212.

[41] He L, et al. M 23 C 6 precipitation behavior in a Ni-base superalloy M963. J Mater Sci 2005;40:2959–64. https://doi.org/10.1007/s10853-005-2418-5.
[42] Sun W, et al. Thermal stability of primary MC carbide and its influence on the performance of cast Ni-base superalloys. Mater Des 2015;69:81–8. https://doi.org/10.1016/j.matdes.2014.12.038.
[43] Liu Y, et al. Microstructure evolution and mechanical performance of nickel based superalloy C1023 at elevated temperatures. Mater Char 2018;138:174–85. https://doi.org/10.1016/j.matchar.2018.01.048.
[44] Klimova M, et al. Cracking behaviour of rené 80-Type superalloy during laser-based directed energy deposition. Metals 2024;14(12):1434. https://doi.org/10.3390/met14121434.
[45] Long A, et al. Creep mechanism and microstructure evolution of a directionally solidified Ni-Based superalloy with different orientations at 850° C. Materials 2025;18(7):1540. https://doi.org/10.3390/ma18071540.
[46] Song X, et al. Analysis of carbide transformation in MC-M23C6 and its effect on mechanical properties of Ni-based superalloy. J Alloys Compd 2022;911:164959. https://doi.org/10.1016/j.jallcom.2022.164959.
[47] Schöberl T, Gupta H, Fratzl P. Measurements of mechanical properties in Ni-base superalloys using nanoindentation and atomic force microscopy. Mater Sci Eng, A 2003;363(1-2):211–20. https://doi.org/10.1016/S0921-5093(03)00627-0.
[48] Napal UG, et al. Thermal mass effect on the solution cooling rate and on HIPped astroloy component properties. Materials 2022;15(4):1434. https://doi.org/10.3390/ma15041434.
[49] Zhou Y, et al. Effects of HIP temperature on the microstructural evolution and property restoration of a Ni-based superalloy. J Mater Eng Perform 2013;22:215–22. https://doi.org/10.1007/s11665-012-0246-8.
[50] Tinga T, Brekelmans W, Geers M. Directional coarsening in nickel-base superalloys and its effect on the mechanical properties. Comput Mater Sci 2009;47(2):471–81. https://doi.org/10.1016/j.commatsci.2009.09.013.